High Power Laser Science and Engineering, (2015), Vol. 3, e6, 13 pages.

doi:10.1017/hpl.2014.50

Temperature dependence of parametric instabilities in the context of the shock-ignition approach to inertial confinement fusion

S. Weber[1] and C. Riconda[2]

[1]*Institute of Physics of the ASCR, ELI-Beamlines, 18221 Prague, Czech Republic*

[2]*LULI, Sorbonne Universités - Université Pierre et Marie Curie - Ecole Polytechnique - CNRS - CEA, 75005 Paris, France*

(Received 24 July 2014; revised 20 November 2014; accepted 2 December 2014)

Abstract

The role of the coronal electron plasma temperature for shock-ignition conditions is analysed with respect to the dominant parametric processes: stimulated Brillouin scattering, stimulated Raman scattering, two-plasmon decay (TPD), Langmuir decay instability (LDI) and cavitation. TPD instability and cavitation are sensitive to the electron temperature. At the same time the reflectivity and high-energy electron production are strongly affected. For low plasma temperatures the LDI plays a dominant role in the TPD saturation. An understanding of laser–plasma interaction in the context of shock ignition is an important issue due to the localization of energy deposition by collective effects and hot electron production. This in turn can have consequences for the compression phase and the resulting gain factor of the implosion phase.

Keywords: inertial confinement fusion; shock ignition; laser–plasma interaction; parametric instabilities

1. Introduction

The principal constituents of shock ignition (SI), converging shocks and their returns in spherical or cylindrical geometry, are based on ideas suggested some time ago[1–3], before it was applied for concrete applications in inertial confinement fusion (ICF)[4–8]. SI is an alternative scheme to ignite pre-compressed fuel in an efficient and robust way, relaxing conditions on the degree of compression and illumination symmetry with respect to standard direct or indirect drive[9–11]. Differently from standard approaches it relies on a short, high-intensity pulse to drive an additional shock which collides with the rebound of the compression shock and allows the creation of a hotspot and thereby ignition of the fuel. Basically SI is a redistribution of the available driver energy by shaping the temporal pulse structure (see Figure 1). This approach decouples target compression from ignition, like fast ignition. It provides a higher target gain/yield for a given laser drive energy. The lower implosion velocity is advantageous for hydrodynamic instabilities. Moreover, SI is less sensitive to hot electrons and fuel preheat. Several experiments regarding the hydrodynamics of SI have been performed already[12–16]. The intensity of the additional shock-inducing spike is of the order of $I\lambda_o^2 \approx 10^{15}$–$10^{16}$ W μm^2 cm^{-2}. This is at least a factor of 10 higher then the laser intensities employed in direct or indirect drive ICF. Strong parametric instability[17] activity such as stimulated Raman backscattering (SRS), stimulated Brillouin backscattering (SBS) and two-plasmon decay (TPD) is likely to be triggered (see Figure 2). The occurrence of inflationary SRS (iSRS)[18] is also likely. Laser–plasma interaction (LPI) under SI conditions has been little studied up to now. At these high laser intensities hydrodynamic modelling becomes questionable as the processes involved are of kinetic nature. It is therefore necessary to use, e.g., particle-in-cell (PIC) codes to better understand the laser absorption process in the plasma corona.

One of the important results of kinetic simulations of LPI in the framework of SI is the fact that the laser energy is absorbed not at the critical density via inverse Bremsstrahlung but by collective effects in the low-density plasma corona[19–24]. This affects the gain considerably as far as ignition is concerned[11]. More detailed investigations are required concerning the coupling of kinetic simulation results from LPI and radiation hydrodynamic simulations for the compression and ignition phase. This paper considers in some detail the role of the coronal electron plasma temperature as far as the SI scenario is concerned. It is complementary to previous publications[19, 20], which have mostly concentrated on the fundamental scenario of

Correspondence to: S. Weber. Email: stefan.weber@eli-beams.eu

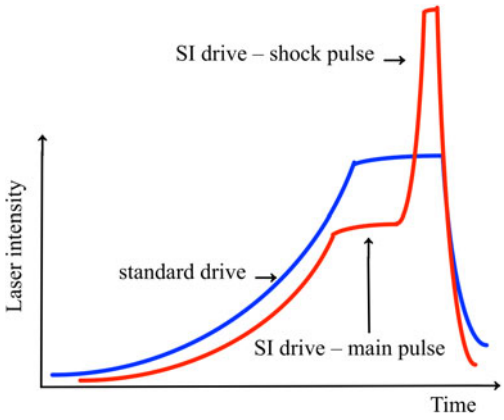

Figure 1. The temporal evolution of the intensity in the case of conventional drive (blue curve) and SI drive (red curve). In the standard approach to ICF the driver is responsible for fuel assembly and a high velocity, $\sim 4 \times 10^7$ cm s^{-1}, for igniting the fuel due to the creation of a hotspot. In the SI scenario the main drive is responsible for fuel assembly but at a lower velocity, $\sim 2 \times 10^7$ cm s^{-1}, preventing ignition. The short high-intensity shock-inducing pulse launched at a later time will reach the fuel at stagnation and ignite it. (Note: the curves in this cartoon drawing are not to scale.)

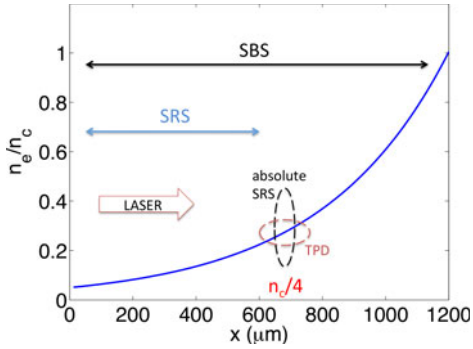

Figure 2. Localization of the various parametric instabilities in the plasma profile. The figure represents a realistic profile. The one used in the simulations is smaller (see Section 2).

Table 1. Summary of the simulations. Here, I_o refers to the laser intensity, T_e is the electron plasma temperature. All simulations are at $3\omega_o$, i.e., a laser wavelength of $\sim$0.3 μm. The fully relativistic PIC code emi2D[42] was used for all simulations; $ZT_i/T_e = 0.2$ for all simulations. The reduced intensity case i8 will not be discussed in the text as the results show the same scenario as the corresponding high-intensity case h8.

Case	$I_o\lambda_o^2$ (W μm^2 cm^{-2})	T_e (keV)
c8	1.2×10^{15}	0.5
h8	1.2×10^{15}	2
h7	1.2×10^{15}	5
h9	1.2×10^{15}	10
i8	4.7×10^{14}	2

parameteric instabilities in the framework of SI. Originally, cavitation at the quarter critical density was identified as a fundamental aspect of LPI for the kind of parameter regime used in the simulations. The present work shows that this phenomenon is strongly temperature dependent. Similarly, the relative production of hot electrons by SRS and TPD is affected by the electron temperature. The coronal plasma temperature is therefore an important issue as present-day preliminary experiments for SI-LPI operate in a regime of lower electron temperature. The coronal plasma electron temperature is expected to be of the order of $\sim$5 keV, whereas the installations used for LPI in the context of SI achieve much less at present (LULI: $\sim$1 keV; PALS: $\leqslant$1 keV; LIL: $\sim$2 keV; OMEGA: $\geqslant$2 keV). Care has to be taken when extrapolating physics behaviour from low temperature to the higher operating temperature expected for SI.

Most of the experimental activity initially concentrated on the hydrodynamic aspects of SI. However, in recent years, several experiments have been performed of relevance or at least related to LPI aspects of SI[10]. Experiments have been performed that concern beam propagation[25–27], SBS[25, 28–35], SRS[36–39] and TPD (Refs. [40, 41] and references therein). It seems that in general energy losses due to backscattering are dominated by Brillouin rather than Raman. The creation of hot electrons by TPD and SRS at the quarter critical density has been observed. The main problem is that one has to fulfil simultaneously the conditions imposed by plasma scale length, electron temperature and laser intensity, as given by possible future experiments on ignition-scale facilities such as NIF and LMJ. Therefore, it is difficult to be conclusive as far as the present experimental effort is concerned. The present experiments should be compared carefully with multi-dimensional kinetic simulations in order to benchmark the codes and to make predictive simulations for the SI parameters.

The remainder of this paper is organized as follows. Section 2 describes the setup for the kinetic simulations using a PIC approach. The results are presented in Section 3 with respect to reflectivity, parametric instabilities, cavitation and the generation of hot electrons. A conclusion is presented in Section 4.

2. Simulation setup

The simulations used in this paper are summarized in Table 1. All simulations are two-dimensional using a full speckle with a Gaussian transverse size of $\sim$24 μm FWHM. A mass ratio $m_i/m_e = 3672$ is used and the ion charge is $Z = 1$. The total simulation time is of the order of $1.5 \times 10^4 \omega_o^{-1} \approx 5$ ps. Radiation hydrodyamic simulations show that the temperature varies little in the plasma corona. Therefore the same temperature is assigned for the whole plasma profile.

https://doi.org/10.1017/hpl.2014.50 Published online by Cambridge University Press

The simulation box is $3600\,k_o^{-1}$ in the parallel direction (laser propagation direction) and $2160\,k_o^{-1}$ in the transverse direction. For a wavelength of ∼0.3 μm this corresponds to ∼172 μm by ∼103 μm. The simulated plasma fills the box completely in the transverse direction but has a length of only ∼148 μm in the parallel direction, being surrounded by a vacuum region on both side. The plasma profile is exponential in the propagation direction of the laser with a scale length of $L_n = (\mathrm{d}\ln n/\mathrm{d}x)^{-1} \approx 60\,\mu\mathrm{m}$ and extends from $0.04\,n_c$ up to $0.4\,n_c$ with 60 particles per cell at the highest density. It should be noted that in reality the gradient scale length is of the order of a few hundred microns. However, previous simulations in 1D have shown that L_n does not affect the underlying scenario and physics strongly but only affects the time scales. The plasma temperature is a much more stringent parameter for LPI-SI simulations then the gradient scale length. The boundary conditions are periodic in the transverse direction and open in the parallel direction. The incident laser light is p-polarized in normal incidence. The pulse length is infinite with a ramp-up time of a few laser cycles. The spatial discretization is $\Delta x = 0.18\,k_o^{-1}$ (in the laser propagation direction), $\Delta y = 0.18\,k_o^{-1}$ (in the transverse direction) and $\Delta t = 0.18\,\omega_o^{-1}$, respecting the Courant–Friedrichs–Lewy condition for explicit integration of the PIC equations. Relativistic normalization is used throughout, i.e., the time t and spatial coordinate x, y are normalized by the laser frequency ω_o and vacuum k-vector k_o, respectively. Collisions are not accounted for. The simulation times are too short and the temperatures too high for collisions to have much of an effect on the parametric instabilities analysed in the following simulations. The typical electron–ion collision frequency is given as $\gamma_{\mathrm{coll}}/\omega_o = 2.74\times10^{-5}(n_e/n_c)\ln\Lambda_{ei}Z/(\lambda_o T_e^{3/2})$, with λ_o in μm and T_e in keV. The use of, as worst-case scenario, the highest plasma density, $0.4\,n_c$, and the lowest temperature, 500 eV, employed in the simulations results in a collision time of $\tau_{\mathrm{coll}} = 1/\gamma_{\mathrm{coll}} \approx 3\times10^4\,\omega_o^{-1}$. This is twice the simuation time. Moreover, for the considered intensities the growth rates of the instabilities are also much larger than the typical collision frequencies.

Figure 3 shows the plasma profile and the transverse cut of the full speckle used in the simulations. The Gaussian profile is cut at 2.67 × FWHM in order to avoid numerical boundary effects.

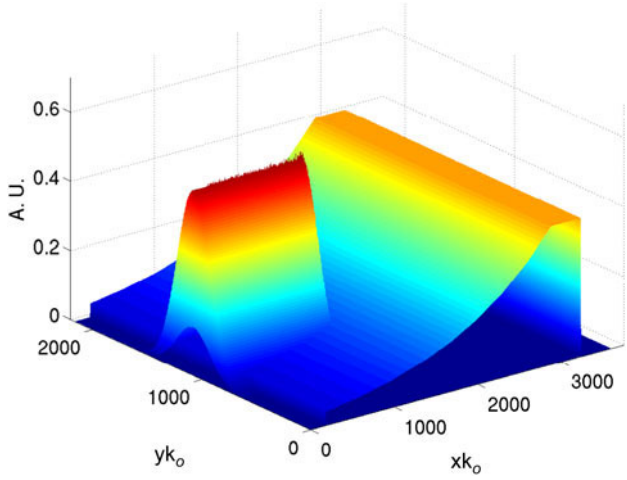

Figure 3. The profiles of the plasma and the incident laser beam. The parameters are given in Section 2.

3. Analysis of simulation results

3.1. Characterization of the parametric instabilities involved

The two main instabilities of interest here are SRS and TPD instability. The resonant SRS process consists of the decomposition of a laser photon (ω_o) into a backscattered frequency-downshifted photon (ω_1) and a forward travelling electron plasma wave (ω_p) (EPW). It fulfils the following conditions for the frequency and wavevector:

$$\begin{aligned}\omega_o &= \omega_1 + \omega_p\\ \mathbf{k}_o &= \mathbf{k}_1 + \mathbf{k}_p.\end{aligned} \tag{1}$$

The frequency of the EPW follows from the dispersion relation as

$$\omega_p \approx \omega_{\mathrm{pe}}(1 + 3k_{epw}^2\lambda_D^2)^{1/2}, \tag{2}$$

where $\omega_{\mathrm{pe}} = (4\pi ne^2/m_e)^{1/2}$ is the local electron plasma frequency and $\lambda_D = v_{\mathrm{the}}/\omega_{\mathrm{pe}} = (kT_e/4\pi ne^2)^{1/2}$ is the Debye length, which in practical units is given as $\lambda_D = 7.43\times10^2 T_e^{1/2}n^{-1/2}$ cm, with T_e in eV and n in cm^3; $v_{\mathrm{the}} = (T_e/m_e)^{1/2}$ is the electron thermal velocity. The electromagnetic k-vector of the backscattered light is given as $k_1 = (\omega_1/c)\sqrt{1-\omega_{\mathrm{pe}}^2/\omega_1^2}$.

The TPD is the decomposition of the laser photon (ω_o) into two plasmons (ω_{p1}, ω_{p2}). The plasmon frequencies are determined by the dispersion relation for the electron plasma waves, Equation (2), and the matching conditions:

$$\begin{aligned}\omega_o &= \omega_{p1} + \omega_{p2}\\ \mathbf{k}_o &= \mathbf{k}_{p1} + \mathbf{k}_{p2}.\end{aligned} \tag{3}$$

Figure 4 shows the geometry of the wavevectors for TPD. The wavevectors of the two plasmons ($\mathbf{k}_1, \mathbf{k}_2$) obey the relations

$$\begin{aligned}\mathbf{k}_{1y} &= -\mathbf{k}_{2y} \equiv \mathbf{k}_y\\ \mathbf{k}_{1,2x} &= \frac{k_o}{2} \pm \Delta\mathbf{k}\\ \Delta\mathbf{k}^2 &= \frac{\mathbf{k}_o^2}{4} + \mathbf{k}_y^2.\end{aligned} \tag{4}$$

https://doi.org/10.1017/hpl.2014.50 Published online by Cambridge University Press

Figure 4. Geometry of the k-vectors involved in the TPD instability. The decay of a photon into two plasmons can be realized in two possible ways while preserving energy and momentum. This particular geometry applies in 2D and helps with the interpretation of the phase space diagrams. In reality, 3D, the number of possible k-vectors is infinite lying on an asymmetric cone around the laser k-vector.

The threshold for the TPD instability in an inhomogeneous plasma profile[43, 44] is temperature dependent and is given as

$$I_{16}^{\mathrm{TPD}} \approx 0.5 T_e L_n^{-1} \lambda_o^{-1}. \tag{5}$$

Here, T_e, is in units of kilo electron volts and I_{16} is the laser intensity in units of 10^{16} W cm^{-2}; L_n and λ_o are given in units of microns. The TPD instability is excited in the vicinity of the quarter critical density and develops as an absolute instability as the slow plasma waves do not escape the resonance. In contrast, the threshold for SRS excitation near $n_c/4$ is not a function of T_e and is given by[17, 45]

$$I_{16}^{\mathrm{SRS}} \approx 12 L_n^{-4/3} \lambda_o^{-2/3}. \tag{6}$$

Depending on the electron temperature, the thresholds for the two instabilities can be quite similar and develop in competition. A high-frequency hybrid instability (HFHI) can develop[46, 47], leading to a co-existence of electrostatic and electromagnetic modes. The growth rate for Raman is given as[48] $\gamma_{\mathrm{SRS}} = \gamma_o \min(1, \gamma_o/\gamma_{\mathrm{tot}})$, with $\gamma_{\mathrm{tot}} = \gamma_L + \gamma_{\mathrm{coll}}$. Here, γ_L and γ_{tot} are the damping rates due to Landau damping and collisions, respectively. In the case when Raman is above threshold, i.e., $\gamma_{\mathrm{SRS}}^2 > \gamma_L \gamma_{\mathrm{coll}}$, the growth rate reduces to $\gamma_{\mathrm{SRS}} = \gamma_o$. Even for the lowest temperature used in the simulations, 500 eV, the collisional damping rate is two orders of magnitude smaller than the Landau damping rate for EPWs, which, for backward SRS, is given as

$$\gamma_L/\omega_o = 0.14 \frac{(n_e/n_c)^{1/2}}{(k_{epw}\lambda_D)^3} \exp(-1/(2k_{epw}^2\lambda_D^2)). \tag{7}$$

Here, $k_{epw} = k_o(\sqrt{1 - n_e/n_c} + \sqrt{1 - 2\sqrt{n_e/n_c}})$ is the electron plasma wavevector and one has the following expression for $k_o^2\lambda_D^2$ in practical units:

$$k_o^2\lambda_D^2 = 1.9 \times 10^{-3} T_e/(n_e/n_c), \tag{8}$$

with T_e in keV. It should be noted that k_o is the value of the electromagnetic wavevector in vacuum.

Evaluation of these expressions at a density of $0.04\, n_c$ and for $T_e = 500$ eV results in a Landau damping rate of $\sim 1 \times 10^{-2}\omega_o^{-1}$, i.e., much larger than the collision rate quoted in Section 2. The largest damping rate will correspond to the largest temperature, 10 keV, and is of the order of $\sim 1 \times 10^{-3}\omega_o^{-1}$ at the quarter critical density $n_e/n_c = 0.25$. However, even in the most damped case, since the collision frequency is so low as discussed in Section 2, the growth rate of Raman remains significantly above threshold and is therefore given by[48]

$$\gamma_{\mathrm{SRS}}/\omega_o = \gamma_o/\omega_o = \frac{(k_{epw}/k_o)(v_{osc}/c)}{2(\sqrt{n_c/n_e} - 1)^{1/2}}, \tag{9}$$

where $v_{osc} = eE_o/\omega_o m_e$ is the quiver velocity of the electrons in the laser electric field. For an intensity of $I\lambda_o^2 = 1.2 \times 10^{15}$ W μm^2 cm^{-2} and a density of $n_e/n_c = 0.25$ one obtains a growth rate for SRS of $\gamma_{\mathrm{SRS}}/\omega_o \approx 1.5 \times 10^{-2}$.

At very low electron plasma temperature, a few hundred eV, the Langmuir decay instability (LDI) can play an important role as it saturates TPD and SRS activity. Although of limited importance in the case of SI which operates in multi-keV conditions, it could be relevant for present-day LPI experiments for SI, as these take place at a much lower temperature. Therefore it is presented in some more detail.

The LDI was predicted in the 1960s[49, 50] and in LPI experiments it was verified more recently by direct observation[36, 51–53], although its experimental existence had already been conjectured before[54], and it has been observed indirectly due to the ion-acoustic wave (IAW) damping on SRS[55–59].

The LDI induces a decay of the pump plasma wave (k_{epw}, ω_p) into an IAW characterized by $(2k_{epw} - \delta k, \omega_{cs})$ (travelling in the direction of the original EPW) and an anti-Stokes daughter EPW (travelling in the opposite direction) having a frequency close to the original frequency (down-shifted by ω_{cs}) and a wavevector given by $k_{epw1} = k_{epw} + \delta k$, where the correction δk has the form

$$\delta k = \tfrac{2}{3}(Zm_e/m_i)^{1/2}/\lambda_D. \tag{10}$$

Here, $\lambda_D = (kT_e/4\pi ne^2)^{1/2}$ is the Debye length, which in practical units is given as $\lambda_D = 7.43 \times 10^2 T_e^{1/2} n^{-1/2}$ cm, with T_e in eV and n in cm^3. A necessary condition for LDI to take place is therefore that[49, 60]

$$k_{epw}\lambda_D > \frac{2}{3}\left(\frac{Zm_e}{m_i}\right)^{1/2} \approx 0.03. \tag{11}$$

For all the cases considered in Table 1 this is clearly the case. However, the higher the temperature, the more the EPWs are damped. The LDI is in general most active at low temperature, provided Equation (11) is fulfilled.

The maximum growth rate is given by

$$\gamma_{\mathrm{LDI}} = \frac{1}{2}\frac{eE_p}{m_e\omega_p}\frac{1}{v_{\mathrm{the}}}\sqrt{\omega_{p1}\omega_{cs}}. \tag{12}$$

https://doi.org/10.1017/hpl.2014.50 Published online by Cambridge University Press

Here, E_p is the electrostatic field associated with the EPWs, ω_p, ω_{p1} represent the two plasmons, and

$$\omega_{cs}^2 = k_{cs}^2 c_s^2 (1/(1 + k_{cs}^2 \lambda_D^2) + 3T_i/ZT_e) \qquad (13)$$

is the IAW frequency. In order for LDI to develop, the growth rate has to be above a threshold given by the linear damping of electron plasma and ion-plasma waves: $\gamma_{\rm LDI} > \sqrt{\gamma_{epw}\gamma_{iaw}}$. In the regime where electron kinetic effects are negligible, LDI, LDI cascade and Langmuir wave collapse tend to dominate the nonlinear evolution of the EPW, participating in the saturation of the SRS instability. If the EPW density fluctuations are below the wavebreaking limit, neglecting the kinetic effect is equivalent to considering $k_{epw}^2 \lambda_D^2 \ll 1$. In such regimes it is thus expected to observe LDI, and its influence on SRS[61–66].

For the intensity considered in this study SBS takes place in the weak-coupling regime even for the lowest temperature used, i.e., Equation (13) is the correct dispersion relation for the IAWs with $k_{cs} \approx 2k_{po}$, with $k_{po} = k_o\sqrt{1 - n_e/n_c}$. The growth rate for SBS in this regime is given as $\gamma_{SBS} = k_{po} v_{osc} \omega_{pi}/\sqrt{2\omega_{cs}\omega_o}$, which in practical units is

$$\gamma_{SBS}/\omega_o = 3.1 \times 10^{-2} \sqrt{I_{16}\lambda_o^2} \left(\frac{n_e}{n_c}\right)^{1/2} \left(\frac{Z}{A}\right)^{1/4} \frac{1}{T_e^{1/4}}. \qquad (14)$$

Here, $\omega_{pi} = \sqrt{4\pi n_i Z^2 e^2/m_i}$ is the ion plasma frequency, Z is the atomic charge and A is the atomic mass number.

In the following the simulation results are analysed with respect to the behaviour of the reflectivity of the incident laser beam, the induced activity of the parametric instabilities, and the phase space and Poynting vector. These issues are of course strongly interdependent.

3.2. Overall scenario

Two fundamental issues have to be addressed as far as the simulations are concerned.

- The relative importance of TPD and SRS. One would expect that the colder the plasma the stronger the TPD.
- Which mechanism is saturating the TPD and SRS activity at the quarter critical density $n_c/4$? Again this will be temperature dependent.

With respect to the first point it is indeed found that the higher the temperature the more pronounced SRS becomes, although it is a negligible energy loss mechanism as far as reflectivity is concerned. With respect to the second point one can observe a clear transition from LDI-induced saturation of Raman at 500 eV to saturation due to cavitation and density fluctuations for temperatures of 2 keV and above. For the low-temperature case c8 there is LDI and TPD activity but no SRS.

SBS is present for any temperature but decreases in importance the higher the temperature. The general conclusion of this set of simulations is that the plasma temperature plays a crucial role as far as the LPI scenario is concerned. Already a factor of two in the electron plasma temperature can significantly affect the relative importance of the parametric instabilities and their effect on the plasma dynamics and laser absorption. Realistic simulations and future experiments for SI require LPI to take place at the right temperature.

The overall energy balance is affected by the amount of the energy of the incident laser beam reflected due to SRS and SBS, Section 3.3, as well as by absorption into collective plasma modes and hot electrons, Sections 3.5 and 3.6. The time scales of the simulations allow study of the saturation of these instabilities related to electron modes, Section 3.4. It has been shown[19, 67] that the development and subsequent saturation of the electron-related instabilities takes place as a recurrent scenario.

3.3. Reflectivity

Figure 5 summarizes the reflectivities for the four temperatures. The reflectivities are evaluated using B_z integrated over the whole transverse direction. The use of B_z instead of E_y ensures that nothing is lost due to a possible opening angle of the backscattered light. There is basically no SRS activity for the cases c8 and h8. The substantial backscattering of the order of 10%–20% originates entirely from Brillouin. Increase of the temperatures strongly reduces SBS activity and increases SRS. However, the energy losses due to SRS even for the highest temperature case, h9, remain negligible. The bursty, spike-like nature of the SRS reflectivity is not related to inflationary SRS, as the corresponding frequency spectra relate the region of SRS activity to the vicinity of $n_c/4$, in accordance with standard absolute SRS excitation. In general, SRS is strongly Landau damped at temperatures of the order of a few keV. However, in the vicinity of the quarter critical density the wavevector of the backscattered light

$$k_1 \approx (1/c)\sqrt{\omega_1^2 - \omega_{\rm pe}^2} = (\omega_o/c)\sqrt{1 - 2\sqrt{n/n_c}} \qquad (15)$$

goes to zero, such that the momentum balance gives $k_{epw} \approx k_o$. The resulting Landau damping rate, see Equations (7) and (8), is of the order of $\gamma_L/\omega_o \approx 10^{-3}$ (for the highest temperature case h9, $T_e = 10$ keV). The threshold for SRS is independent of temperature, so one would expect that the SRS-induced part of the reflectivity will not change as the temperature is increased. However, locally TPD and SRS are competing for the pump and the threshold for TPD is strongly temperature dependent. As T_e increases, TPD activity is reduced and SRS can take more energy out of the pump, thereby increasing the reflectivity.

https://doi.org/10.1017/hpl.2014.50 Published online by Cambridge University Press

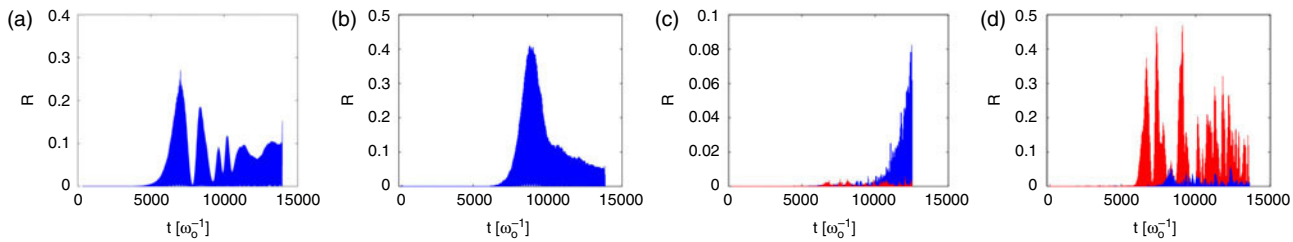

Figure 5. Reflectivities ($R = I/I_o$, i.e., reflected intensity over incident intensity at the centre of the speckle in the transverse direction) for the cases (a) c8, (b) h8, (c) h7 and (d) h9. The curves are 'filled' as the laser temporal period is resolved. The blue curve corresponds to SBS-like frequencies, summing the range $0.9\omega_o$–$1.1\omega_o$. The red curve corresponds to SRS-like frequencies, summing the range $0.0\omega_o$–$0.9\omega_o$. No frequencies are present in the interval $0.8\omega_o$–$0.9\omega_0$. Note: the time on the axis refers to the moment the reflected light crosses the boundary of the computational box; as the quarter critical density is located at $2200\,k_o^{-1}$, the light was actually refelected $\sim 2200\omega_o^{-1}$ earlier.

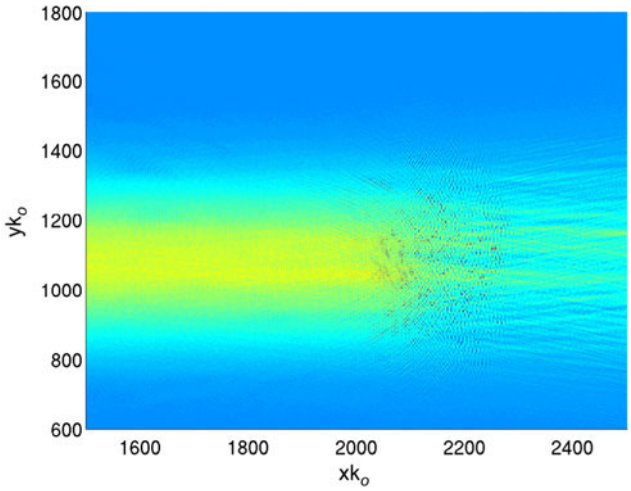

Figure 6. Poynting vector for the case h9 at $t\omega_o = 13\,600$.

The total reflectivities, i.e., the SRS and SBS contributions combined, reduce strongly as the temperature is increased. For the cases c8 and h8 the average reflectivity is of the order of 10%–15%, whereas for the high-temperature cases, h7 and h9, the overall reflectivity is reduced to 1%–2% only.

SBS develops everywhere in the profile, up to $n_c/4$. At $n_c/4$ SBS is strongly inhibited due to the fact that the laser beam is randomized due to the cavitation process and LDI, and the associated strong density fluctuations (see, e.g., Figure 6 for the case h9).

By contrast, SRS develops predominantly at $n_c/4$. The simulated time scales are short for the SBS evolution. It is therefore unclear what the saturation mechanisms for SBS are on longer time scales. The bursty behaviour of the reflectivities as visible in Figure 5 has been observed before and was discussed in the literature[19, 68]. In the case of SRS it is related to hot electron production and cavity creation.

Figure 7 shows the frequency spectra of the backscattered light, in agreement with the decomposition into SRS and SBS of the reflectivities. In the cold case, c8 (Figure 7(a)), the SRS signal is at $0.5\omega_o$ but is very weak in agreement with the reflectivity curves. In the hot case, h9 (Figure 7(b)), SRS is dominant. Clearly visible is a splitting of the SRS frequency around $0.5\omega_o$ with $\Delta k \approx 0.013\,k_o$. This most likely originates from density perturbations induced by TPD and/or cavitation. The localization of the SRS signal around $0.5\omega_o$ is a signature of the fact that SRS originates from the vicinity of the quarter critical density. The downshifted backscattered light from SRS has the correct frequency to be trapped locally in density cavities[19, 20].

Figure 8 shows the Fourier transforms of the electromagnetic field in the plasma for the two extreme cases, c8 and h9. In Figure 8(a) one can observe a feature at $|k| = 1.5\,k_o$ at large angle. This is a signature of TPD coupling with the laser and disappears at later time after saturation of TPD, as can be seen in Figure 8(b). The signal close to $0.86\,k_o$ stems from the incoming laser and the backscattered light due to SBS. The strong-signal opening angle increases in time due to side scattering and refraction from density perturbations. In the hot case, Figure 8(b, d), at later time two pronounced signals appear at $k_\parallel \approx 0.05\,k_o$ and $k_\parallel \approx 1.5\,k_o$. The first is the signature of SRS, as $k_1 \ll 1$ close to $n_c/4$ (see the discussion above), the latter one is the coupling of electron plasma waves at $\omega \approx 0.5\omega_o$ with the laser. As expected, the signal is mostly in the parallel direction as SRS has a small opening angle.

3.4. Electron-related mode activity: SRS, TPD and LDI

As already mentioned, there is almost no SRS for the cases c8 and h8. Strong SRS is present for higher temperatures above 2 keV. In general, it can be said that there is no SRS activity in the low-density part of the plasma corona. SRS is concentrated near the quarter critical density. The high-temperature case h9 has very strong absolute SRS activity but basically no TPD.

As can be seen from Table 2, the threshold for TPD is much lower then the threshold for SRS for the cases c8 and h8. As a consequence, TPD arises first and no or very little absolute SRS develops as TPD is initially depleting the

https://doi.org/10.1017/hpl.2014.50 Published online by Cambridge University Press

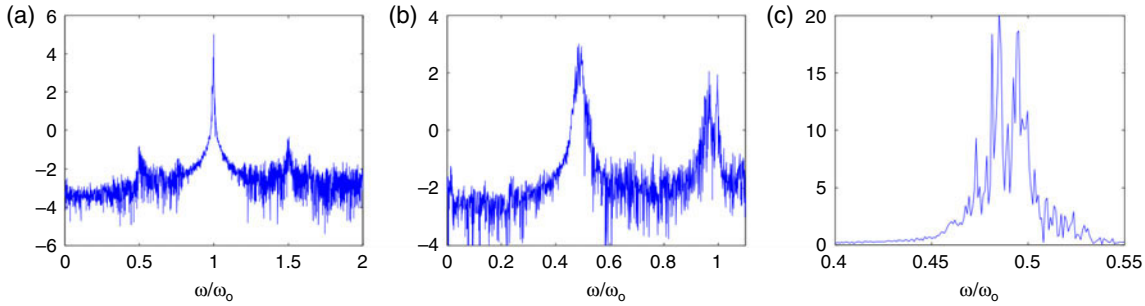

Figure 7. Frequency spectra for the cases (a) c8, (b) h9 and (c) a zoom of (b). Note: (a) and (b) are on log scale whereas (c) is on linear scale.

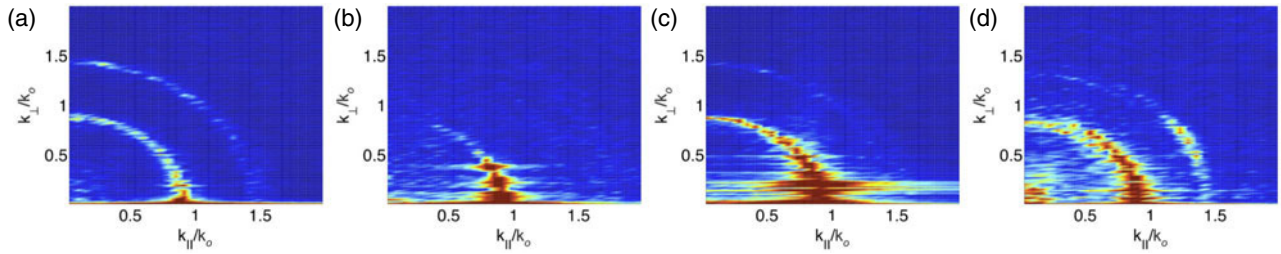

Figure 8. Two-dimensional Fourier spectra of the electromagnetic field B_z evaluated in the vicinity of $n_c/4$ for the cases c8 (a, c) and h9 (b, d) taken at times $t\omega_o = 4000$ (a, b) and $t\omega_o = 7000$ (c, d).

Table 2. Temperature-dependent occurrence of LPI phenomena. The number of stars gives a rough 'visual' interpretation of the strength of the process occurring, with ⋆ ⋆ ⋆⋆ strongest and ⋆ weakest. The numbers in the columns I_{16}^{TPD} and I_{16}^{SRS} are calculated from the corresponding Equations (5) and (6). The thresholds have to be compared with the laser intensity, which in units of 10^{16} W cm^{-2} is 1.2 for all cases. CAV = cavitation.

Case	T_e (keV)	CAV	LDI	SRS	SBS	TPD	I_{16}^{TPD}	I_{16}^{SRS}
c8	0.5	⋆	⋆ ⋆ ⋆⋆	⋆	⋆ ⋆ ⋆⋆	⋆ ⋆ ⋆⋆	0.014	0.11
h8	2	⋆⋆	⋆ ⋆ ⋆	⋆	⋆ ⋆ ⋆⋆	⋆ ⋆ ⋆⋆	0.056	0.11
h7	5	⋆ ⋆ ⋆⋆	⋆	⋆ ⋆ ⋆	⋆⋆	⋆ ⋆ ⋆	0.14	0.11
h9	10	⋆ ⋆ ⋆⋆	⋆	⋆ ⋆ ⋆⋆	⋆	⋆⋆	0.28	0.11

pump, as can be seen in Figure 9. The figure clearly shows the absence of any laser beam in the density profile behind the quarter critical density, which however is a transient feature due to TPD saturation.

As the SBS reflectivity data (see Figure 5(a)) show reflection of about 20%–30%, the remaining energy of order 70% at this time is absorbed in the plasma due to TPD.

At a later stage SRS still does not develop due to the strong, irregular small-scale density modulations induced by TPD. For the cold case c8, TPD is saturated by LDI which develops on the EPWs generated originally by TPD.

In the high-temperature cases (h7 and h9) the threshold for SRS is lower than for TPD and strong absolute SRS develops which induces cavitation and leads to saturation.

Figure 10(a) shows the Fourier transform of the ion density for the coldest case, c8, after TPD saturation. The large feature between 30° and 40° reproduces the IAWs which are the result of LDI decay of the plasmons excited by TPD and has k-vectors that are roughly twice the original k-vectors from the EPWs. The extent is due to the large spread of the k-vectors of the EPWs. The smaller feature with $k_\parallel$ close to zero results from the low-frequency beating of symmetrically excited plasmons, e.g., EPW_1 and EPW'_1 in Figure 4, summing up to purely perpendicular fluctuations[69]. The very small feature at $k_\parallel \approx 1.8\,k_o$ and in an almost perfect forward direction is the IAW signal generated by SBS (also visible in (b) for case h8).

The EPWs generated by TPD and the secondary waves generated by LDI evolve into turbulence, as observed in other recent simulations for SI[18, 70–72] (see the discussion of real-space figures in Section 3.5). As the temperature increases (Figure 10(b–d)), the LDI-induced signal disappears and the purely perpendicular signal from the EPW beating retreats to smaller wavevector (longer wavelength).

3.5. Plasma cavitation

The role of cavitation was clearly identified in previous work related to SI[19–21]. It is a fundamental mechanism of LPI which acts as a converter, transferring energy from the laser into kinetic energy of the plasma, and was originally identified in SBS activity[73]. Cavities present strong local plasma perturbations which can act as a dynamic random phase plate and induce coherence loss to the incident laser beam, i.e., they act as a means of plasma smoothing[68].

https://doi.org/10.1017/hpl.2014.50 Published online by Cambridge University Press

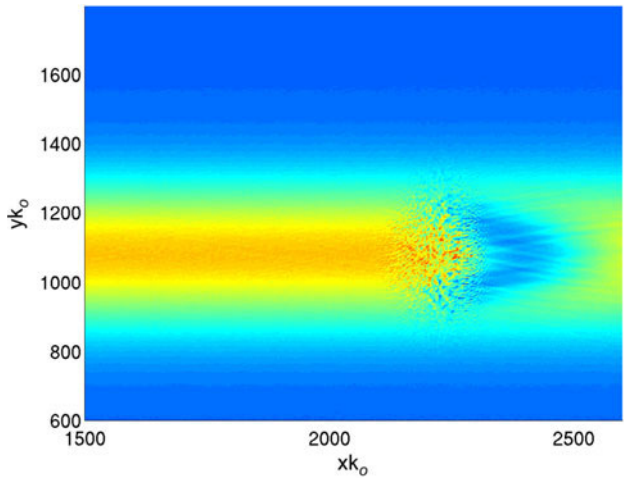

Figure 9. Poynting vector for the case c8 at $t\omega_o = 3600$. The 'hole' behind the density layer around $n_c/4$ is clearly visible.

They are also essential in saturating parametric instabilities at the quarter critical density. Finally, they are an important mechanism for laser energy absorption. Figure 11 shows the ion density cavities for the various simulation cases. As was shown before[19], the presence of the beating of the TPD waves facilitates the cavitation process. As the threshold for TPD is a linear function of T_e, see Equation (5), one would expect cavitation to occur later, the higher the temperature is. This is confirmed by the figure, which shows for each of the cases the time slice of maximum cavity activity. The cavities can be filled with either electrostatic[71, 72] or electromagnetic fields; for high laser intensity it was shown that they have a soliton-like structure[19, 20].

The high-temperature case h9, in particular, Figure 11(d), shows very large crater remnants from previous cavitations. These density perturbations strongly affect the incident laser light and act as a dynamic random phase plate, inducing fluctuating speckles for densities above $n_c/4$ (see Figure 6), thereby randomizing the laser beam that is transmitted across the perturbed density layer. In previous work it was established that SRS-induced cavitation and TPD might help the cavitating process by providing initial density modulation which serves as seeds for SRS-induced cavitation. In this particular case the characteristic size of the cavities is of the order of the laser wavelength, which is in contrast to electrostatic cavities having typical sizes of the order of some λ_D. The particular regimes where either one or the other is dominant are not yet fully clarified.

As discussed above (see Section 3.4), SRS activity increases with increasing temperature (also observed in Ref. [67]) at the quarter critical density. At the same time

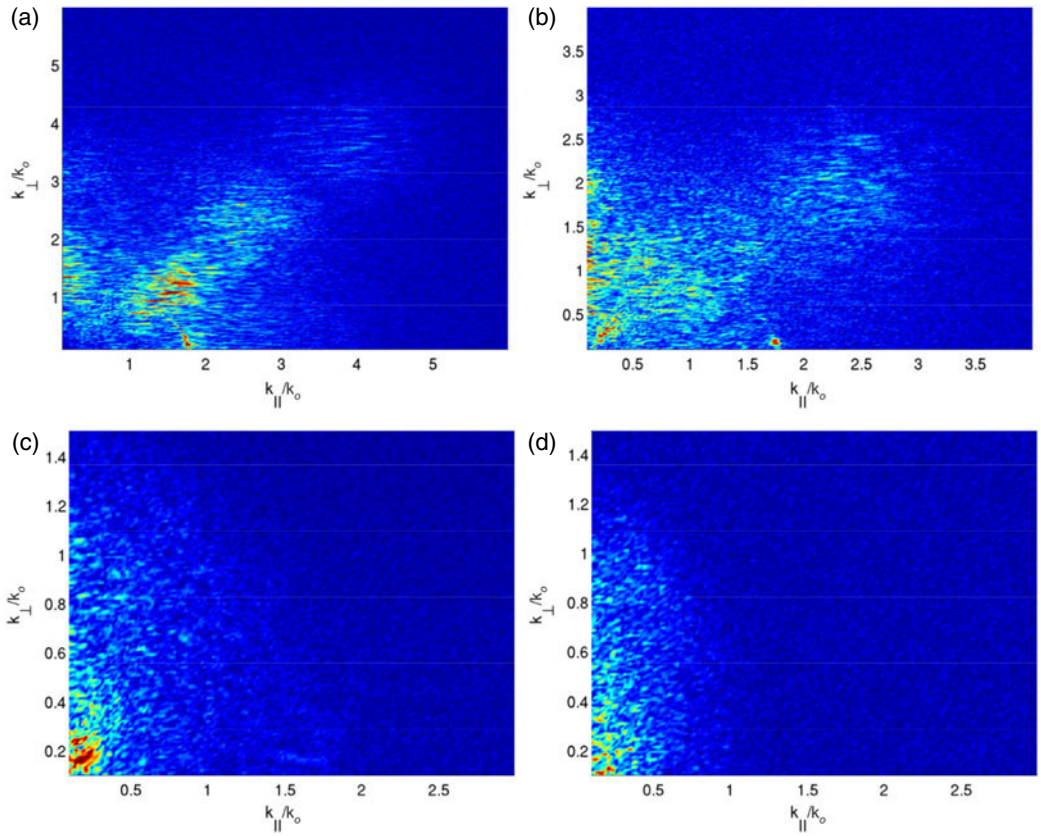

Figure 10. Fourier transform of the ion density corresponding to Figure 11. (a) Case c8 at $t\omega_o = 5600$, (b) case h8 at $t\omega_o = 7000$, (c) case h7 at $t\omega_o = 8300$ and (d) case h9 at $t\omega_o = 13\,600$. It should be noted that the axes for the various cases differ as the k-vectors become shorter as the temperature increases.

https://doi.org/10.1017/hpl.2014.50 Published online by Cambridge University Press

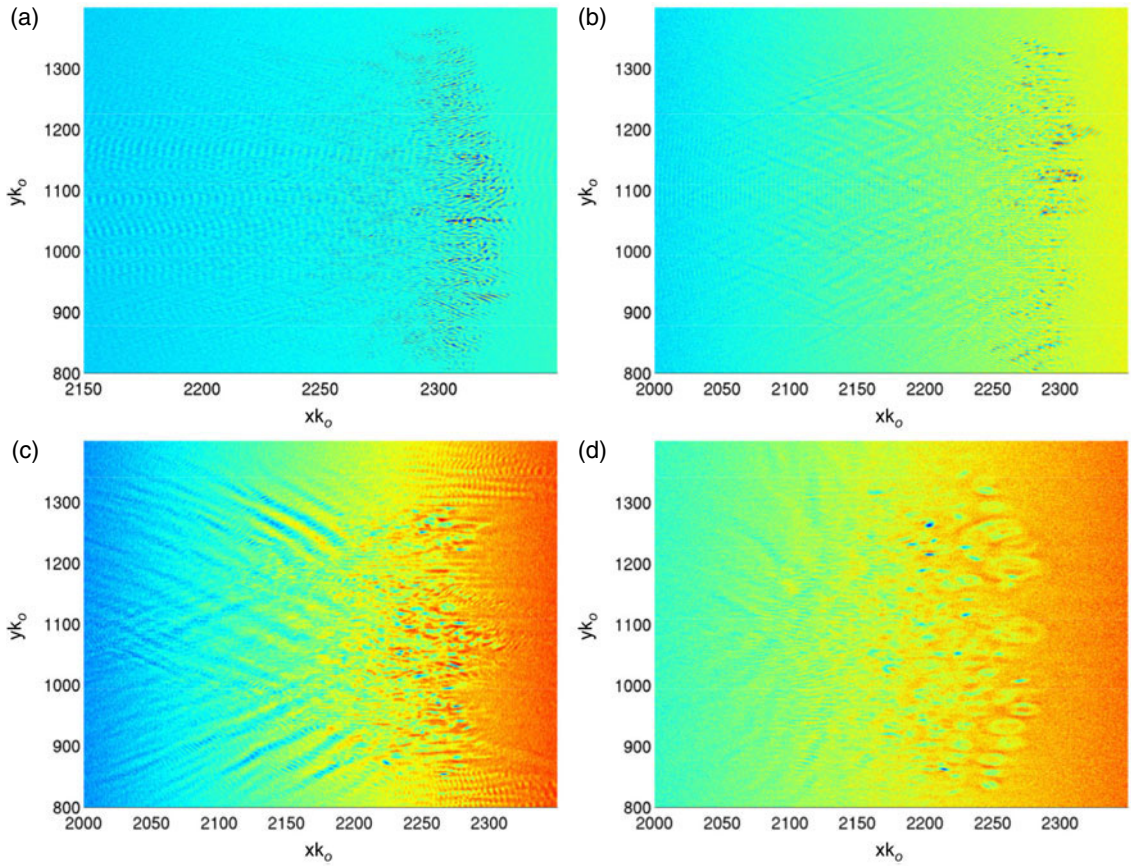

Figure 11. Ion density near the quarter critical density (located at $xk_o \approx 2300$. (a) Case c8 at $t\omega_o = 5600$, (b) case h8 at $t\omega_o = 7000$, (c) case h7 at $t\omega_o = 8300$ and (d) case h9 at $t\omega_o = 13\,600$. It should be noted that the colour scale used is not the same for each of the four sub-figures in order to enhance the visibility of the structures.

this also increases cavitation activity and size, as visible in Figure 11(a–d). In addition, a higher temperature implies a higher laser intensity such that the ponderomotive force can balance the plasma pressure so that cavities can be maintained.

The creation of the cavities is therefore an intricate interdependence of laser intensity, plasma profile, plasma temperature and growth rate of absolute Raman at $n_c/4$. From previous and present simulations it follows that the optimum is around 5 keV for cavity creation. Figure 11(c) has more cavities than the 10 keV case shown in Figure 11(d). The reason for this is that the TPD activity for the case h9 is reduced due to the higher threshold for exciting the instability, which, as said, facilitates the creation of cavities. The typical lifetime of these cavities is of the order of picoseconds, which implies that they are a recursive phenomenon.

3.6. Laser absorption into hot electrons

SRS, TPD and cavitation are all sources of hot electron production. However, the hot electrons differ as far as temperature and propagation direction are concerned[19, 20].

As discussed above, TPD is the dominant process in the cold case c8. As shown in Figure 4, the decay takes place in two directions, which is reflected in the phase space of the electrons, Figure 12(a). Clearly visible are the emerging clouds of accelerated electrons in the forward and backward directions. The presence of two partially separated features in phase space can be related to the excitation of plasma waves centred around different k-vectors, which has also been observed recently in other simulation work[74]. A corresponding signature is found in the p_y-space (not shown here). By contrast, the hot case h9, Figure 12(d), shows only a strong signature of SRS-accelerated electrons in the forward direction. No clear signal from TPD is visible. The intermediate cases, h7 and h8, show contributions from both processes, TPD and SRS. Most of the incident laser energy at this stage is absorbed in the vicinity of $n_c/4$ by either collective modes or hot electrons. For the case c8, Figure 9, depletion of the pump occurs after $2300\omega_o^{-1}$, i.e., no transmission at all. At early time the transmissivity is on average 50%, and it is 10% at later time (around $\sim 7000\omega_o^{-1}$). For case h8 one has 35% transmission at early time, and 15% at later time (same times as for the previous case c8). The case h7 is shown in detail in Figure 2(b) of Ref. [19]

https://doi.org/10.1017/hpl.2014.50 Published online by Cambridge University Press

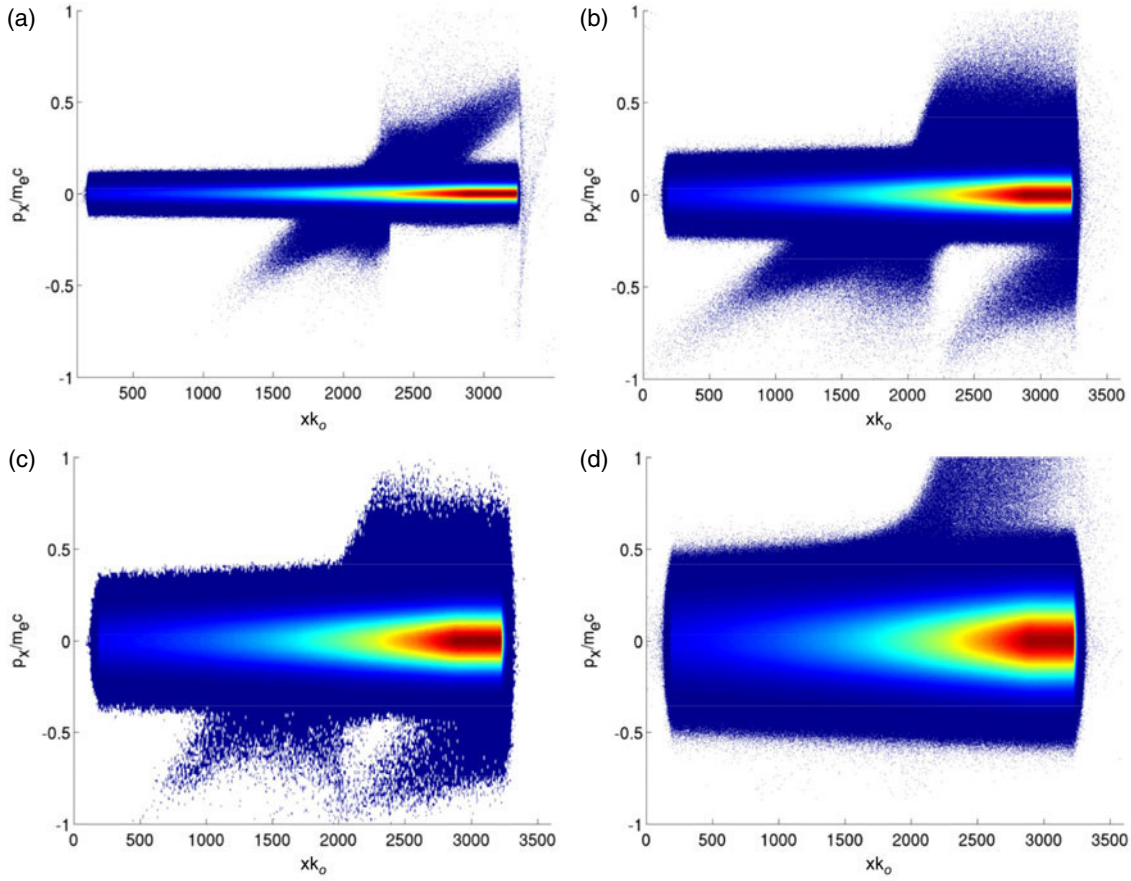

Figure 12. The transverse electron phase space as a function of the laser propagation direction for (a) case c8 at $t\omega_o = 5600$, (b) case h8 at $t\omega_o = 7000$, (c) case h7 at $t\omega_o = 7400$ and (d) case h9 at $t\omega_o = 5200$. The time slice for h9 is taken at an early time as the electrons start to recirculate quickly.

and has roughly 50% transmission. Finally, for the case h9 one has 25%–30% transmission increasing towards the end of the simulation. The hot electrons also act as a damping mechanism for EPWs and participate in the saturation of TPD and SRS. The distribution functions and temperatures are similar to those obtained previously[19, 20].

As was pointed out previously[10], the temperature characterizing the hot tail of the electron distribution function is less than 100 keV and is not dependent on the laser intensity but is determined by the resonant interaction of the electrons with the plasma waves generated by TPD and SRS. The laser intensity affects the number of hot electrons produced. The relevant parameters affecting the hot electron production are the phase velocity and the initial bulk electron temperature. Present and previous simulation work[19, 20] indicates that the hot electron temperature increases with the initial bulk temperature of the plasma. However, a more detailed analysis would be required to quantify this relationship.

4. Conclusions

The relative importance of the various phenomena (cavitation, LDI, SRS, SBS and TPD) is summarized in Table 2 in a qualitative way. The ratio between the thresholds for SRS and TPD is roughly $I^{\mathrm{SRS}}/I^{\mathrm{TPD}} \approx (24/T_e)(\lambda/L_n)^{1/3}$. Setting the ratio equal to 1 results in an electron plasma temperature of ≈4.3 keV, which separates the SRS-dominated regime from the TPD-dominated regime. This value agrees well with the observed switchover of the LPI scenario in the simulations. The laser intensities used in the simulations are above the threshold intensities for SRS and TPD for all temperatures used in the simulations. One should note that the above ratio depends strongly on the plasma temperature but only weakly on the gradient scale length of the plasma profile. Therefore, temperature should be the determining parameter for a given intensity. On increasing the intensity other instabilities might appear, such as iSRS in the low-density region, far below $n_c/4$, although saturation of SRS and TPD close to $n_c/4$ was observed. In addition, SBS will become even more dominant on the time scales considered in the simulations[19, 20]. Intensities higher than the ones considered here are not *a priori* excluded for the SI scenario and should motivate further studies in this respect.

An important conclusion of the simulation work presented is the necessity to have better absorption models for the laser beam in radiation hydrodynamic simulation for shock

https://doi.org/10.1017/hpl.2014.50 Published online by Cambridge University Press

ignition. It is clear that a large fraction, or even most of it, dependent on the LPI parameters, is not absorbed via inverse Bremsstrahlung at the critical density, but rather by collective effects in the low-density corona. This has to be accounted for in hydrodynamic simulations of the implosion phase in a realistic way. Reliable integrated simulations for SI are necessary.

SI experiments and simulations therefore currently have some important caveats.

- The sensitivity of the participating LPI instabilities as far as the coronal plasma temperature is concerned limits the validity of experimental investigations; extrapolation to higher T_e than can be achieved on medium-size installations such as LULI, PALS, LIL or OMEGA requires particular care.
- The largest energy losses due to backscattering in the few-keV range come from SBS and not from SRS. Many SI-relevant present-day experiments concentrate on Raman rather than Brillouin.
- An open issue is the saturation mechanism for SBS which operates on time scales of at least tens of picoseconds.
- Longer time scales are required for kinetic LPI simulations. This was partially addressed by recent work[67].

Another important issue is how these instabilities are affected in the case of multiple overlapping beams as the driver[75].

Much more detailed experiments and simulations are needed to determine the presence and relative importance of the various participating instabilities.

A very interesting issue is to determine experimentally where exactly the laser energy is absorbed: in the low-density plasma corona, at the critical surface or at both locations (in which case the ratio would be important). Possible hot electrons have to be attributed clearly to either SRS or TPD. The distribution functions and directionality of the hot electrons will help in this respect. The simulations clearly show the importance of cavitation at the quarter critical density. The cavities are in general of the order of a few wavelengths. It should be possible to perform interferometry at $4\omega_o$ to image the presence of cavities.

Acknowledgements

Use of the computing center CCRT of the *Commissariat à l'énergie atomique et aux énergies alternatives* is acknowledged. C.R. acknowledges support from grant ANR-11-IDEX-0004-02 Plas@Par. S.W. benefitted from the support of the Czech Science Foundation (Project No. CZ.1.07/2.3.00/20.0279) and from ELI (Project No. CZ.1.05/1.1.00/02.0061).

References

1. G. von Guderley, Luftfahrt-Forsch. **9**, 302 (1942).
2. K. Brueckner and S. Jorna, Rev. Mod. Phys. **46**, 325 (1974).
3. V. Shcherbakov, Sov. J. Plasma Phys. **9**, 240 (1983).
4. R. Betti, C. Zhou, K. Anderson, L. Perkins, W. Theobald, and A. Solodov, Phys. Rev. Lett. **98**, 155001 (2007).
5. L. Perkins, R. Betti, K. LaFortune, and W. Williams, Phys. Rev. Lett. **103**, 045004 (2009).
6. X. Ribeyre, G. Schurtz, M. Lafon, S. Galera, and S. Weber, Plasma Phys. Control. Fusion **51**, 015013 (2009).
7. X. Ribeyre, M. Lafon, G. Schurtz, M. Olazabal-Loume, J. Breil, S. Galera, and S. Weber, Plasma Phys. Control. Fusion **51**, 124030 (2009).
8. X. Ribeyre, S. Guskov, J.-L. Feugeas, P. Nicolai, and V. Tikhonchuk, Phys. Plasmas **20**, 062705 (2013).
9. S. Atzeni, X. Ribeyre, G. Schurtz, A. Schmitt, B. Canaud, R. Betti, and L. Perkins, Nucl. Fusion **54**, 054008 (2014).
10. D. Batani, S. Baton, A. Casner, S. Depierreux, M. Hohenberger, O. Klimo, M. Koenig, C. Labaune, X. Ribeyre, C. Rousseaux, G. Schurtz, W. Theobald, and V. Tikhonchuk, Nucl. Fusion **54**, 054009 (2014).
11. M. Temporal, B. Canaud, W. Garbett, R. Ramis, and S. Weber, High Power Laser Sci. Eng. **2**, e8 (2014).
12. W. Theobald, K. Anderson, R. Betti, R. Craxton, J. Delettrez, J. Frenje, V. Glebov, O. Gotchev, J. Kelly, C. Li, A. Mackinnon, F. Marshall, R. McCrory, D. Meyerhofer, J. Myatt, P. Norreys, P. Nilson, P. Patel, R. Petrasso, P. Radha, C. Ren, T. Sangster, W. Seka, V. Smalyuk, A. Solodov, R. Stephens, C. Stoeckl, and B. Yaakobi, Plasma Phys. Control. Fusion **51**, 124052 (2009).
13. W. Theobald, R. Nora, M. Lafon, A. Casner, X. Ribeyre, K. Anderson, R. Betti, J. Delettrez, J. Frenje, V. Glebov, O. Gotchev, M. Hohenberger, S. Hu, F. Marshall, D. Meyerhofer, T. Sangster, G. Schurtz, W. Seka, V. Smalyuk, C. Stoeckl, and B. Yaakobi, Phys. Plasmas **19**, 102706 (2012).
14. S. Baton, M. Koenig, E. Brambrink, H. Schlenvoigt, C. Rousseaux, G. Debras, S. Laffite, P. Loiseau, F. Philippe, X. Ribeyre, and G. Schurtz, Phys. Rev. Lett. **108**, 195002 (2012).
15. M. Hohenberger, W. Theobald, S. Hu, K. Anderson, R. Betti, T. Boehly, A. Casner, D. Fratanduono, M. Lafon, D. Meyerhofer, R. Nora, X. Ribeyre, T. Sangster, G. Schurtz, W. Seka, C. Stoeckl, and B. Yaakobi, Phys. Plasmas **21**, 022702 (2014).
16. D. Batani, M. Koenig, S. Baton, F. Perez, L. Gizzi, P. Koester, L. Labate, J. Honrubia, L. Antonelli, A. Morace, L. Volpe, J. Santos, G. Schurtz, S. Hulin, X. Ribeyre, C. Fourment, P. Nicolai, B. Vauzour, L. Gremillet, W. Nazarov, J. Pasley, M. Richetta, K. Lancaster, C. Spindloe, M. Tolley, D. Neely, M. Kozlova, J. Nejdl, B. Rus, J. Wolowski, J. Badziak, and F. Dorchies, Plasma Phys. Control. Fusion **53**, 124041 (2011).
17. W. Kruer, *The Physics of Laser–Plasma Interaction* (Addison Wesley, New York, 1988).
18. H. Vu, D. DuBois, and B. Bezzerides, Phys. Rev. Lett. **86**, 4306 (2001).
19. C. Riconda, S. Weber, V. Tikhonchuk, and A. Heron, Phys. Plasmas **18**, 092701 (2011).
20. S. Weber, C. Riconda, O. Klimo, A. Heron, and V. Tikhonchuk, Phys. Rev. E **85**, 016403 (2012).
21. O. Klimo, S. Weber, V. Tikhonchuk, and J. Limpouch, Plasma Phys. Control. Fusion **52**, 055013 (2010).

https://doi.org/10.1017/hpl.2014.50 Published online by Cambridge University Press

22. O. Klimo, V. Tikhonchuk, X. Ribeyre, G. Schurtz, C. Riconda, S. Weber, and J. Limpouch, Phys. Plasmas **18**, 082709 (2011).
23. O. Klimo and V. Tikhonchuk, Plasma Phys. Control. Fusion **55**, 095002 (2013).
24. O. Klimo, J. Psikal, V. Tikhonchuk, and S. Weber, Plasma Phys. Control. Fusion **56**, 055010 (2014).
25. S. Depierreux, C. Labaune, D. Michel, C. Stenz, P. Nicolaï, M. Grech, G. Riazuelo, S. Weber, C. Riconda, V. Tikhonchuk, P. Loiseau, N. Borisenko, W. Nazarov, S. Hüller, D. Pesme, M. Casanova, J. Limpouch, C. Meyer, P. DiNicola, R. Wrobel, E. Alozy, P. Romary, G. Thiell, G. Souillié, C. Reverdin, and B. Villette, Phys. Rev. Lett. **102**, 195005 (2009).
26. J. Moody, B. MacGowan, D. Hinkel, W. Kruer, E. Williams, K. Estabrook, R. Berger, R. Kirkwood, D. Montgomery, and T. Shepard, Phys. Rev. Lett. **77**, 1294 (1996).
27. S. Depierreux, K. Lewis, C. Labaune, and C. Stenz, J. Phys. IV **133**, 317 (2006).
28. S. Depierreux, P. Loiseau, D. Michel, V. Tassin, C. Stenz, P.-E. Masson-Laborde, C. Goyon, V. Yahia, and C. Labaune, Phys. Plasmas. **19**, 012705 (2012).
29. C. Labaune, K. Lewis, H. Bandulet, S. Depierreux, S. Huller, P. Masson-Laborde, D. Pesme, and G. Riazuelo, J. Phys. IV **133**, 29 (2006).
30. H. Baldis, C. Labaune, J. Moody, T. Jalinaud, and V. Tikhonchuk, Phys. Rev. Lett. **80**, 1900 (1998).
31. R. Drake, R. Watt, and K. Estabrook, Phys. Rev. Lett. **77**, 79 (1996).
32. J. Fernandez, B. Bauer, K. Bradley, J. Cobble, D. Montgomery, R. Watt, B. Bezzerides, K. Estabrook, R. Focia, S. Goldman, D. Harris, E. Lindman, H. Rose, J. Wallace, and and B. Wilde, Phys. Rev. Lett. **81**, 2252 (1998).
33. H. Baldis, C. Labaune, E. Schifano, N. Renard, and A. Michard, Phys. Rev. Lett. **77**, 2957 (1996).
34. C. Goyon, S. Depierreux, D. Michel, G. Loisel, V. Yahia, P. Masson-Laborde, P. Loiseau, S. Huller, N. Borisenko, A. Orekhov, O. Rosmej, P. Nicolai, V. Tikhonchuk, and C. Labaune, EPJ Web Conf. **59**, 05006 (2013).
35. C. Goyon, S. Depierreux, V. Yahia, G. Loisel, C. Baccou, C. Courvoisier, N. Borisenko, A. Orekhov, O. Rosmej, and C. Labaune, Phys. Rev. Lett. **111**, 235006 (2013).
36. D. Michel, S. Depierreux, C. Stenz, V. Tassin, and C. Labaune, Phys. Rev. Lett. **104**, 255001 (2010).
37. L. Antonelli, D. Batani, A. Patria, O. Ciricosta, C. Cecchetti, P. Koester, L. Labate, A. Giulietti, L. Gizzi, A. Moretti, M. Richetta, L. Giuffrida, L. Torrisi, M. Kozlova, J. Nejdl, M. Sawicka, D. Margarone, B. Rus, G. Schurtz, X. Ribeyre, M. Lafon, C. Spindloe, and T. O'Dell, Acta Tecn. **56**, T57 (2011).
38. S. Depierreux, C. Goyon, K. Lewis, H. Bandulet, D. T. Michel, G. Loisel, V. Yahia, V. Tassin, C. Stenz, N. G. Borisenko, W. Nazarov, J. Limpouch, P. E. Masson Laborde, P. Loiseau, M. Casanova, Ph. Nicolaï, S. Hüller, D. Pesme, C. Riconda, V. T. Tikhonchuk, and C. Labaune, Plasma Phys. Control. Fusion **53**, 124034 (2011).
39. P. Koester, L. Antonelli, S. Atzeni, J. Badziak, F. Baffigi, D. Batani, C. A. Cecchetti, T. Chodukowski, F. Consoli, G. Cristoforetti, R. De Angelis, G. Folpini, L. A. Gizzi, Z. Kalinowska, E. Krousky, M. Kucharik, L. Labate, T. Levato, R. Liska, G. Malka, Y. Maheut, A. Marocchino, P. Nicolai, T. O'Dell, P. Parys, T. Pisarczyk, P. Raczka, O. Renner, Y. J. Rhe, X. Ribeyre, M. Richetta, M. Rosinski, L. Ryc, J. Skala, A. Schiavi, G. Schurtz, M. Smid, C. Spindloe, J. Ullschmied, J. Wolowski, and A. Zaras, Plasma Phys. Control. Fusion **55**, 124045 (2013).
40. H. Baldis and C. Walsh, Phys. Fluids **26**, 1364 (1983).
41. W. Seka, J.-F. Myatt, R. Short, D. Froula, J. Katz, V. Goncharov, and I. Iguminshchev, Phys. Rev. Lett. **112**, 145001 (2014).
42. Code developed by A. Heron and J.-C. Adam at CPHT. Ecole Polytechnique.
43. C. Liu and M. Rosenbluth, Phys. Fluids **19**, 967 (1976).
44. A. Simon, R. Short, E. Williams, and T. Dewandre, Phys. Fluids **26**, 3107 (1983).
45. C. Menyuk, N. El-Siragy, and W. Manheimer, Phys. Fluids **28**, 3409 (1985).
46. B. Afeyan and E. Williams, Phys. Rev. Lett. **75**, 4218 (1995).
47. B. Afeyan and E. Williams, Phys. Plasmas **4**, 3845 (1997).
48. D. Forslund, J. Kindel, and E. Lindman, Phys. Fluids **18**, 1002 (1975).
49. V. Oraevskii and R. Sagdeev, Sov. Phys. Tech. Phys. **7**, 955 (1963).
50. Y. Ichikawa, Phys. Fluids **9**, 1454 (1966).
51. S. Depierreux, J. Fuchs, C. Labaune, A. Michard, H. Baldis, D. Pesme, S. Hüller, and G. Laval, Phys. Rev. Lett. **84**, 2869 (2000).
52. S. Depierreux, C. Labaune, J. Fuchs, D. Pesme, V. Tikhonchuk, and H. Baldis, Phys. Rev. Lett. **89**, 045001 (2002).
53. J. Kline, D. Montgomery, B. Bezzerides, J. Cobble, D. DuBois, R. Johnson, H. Rose, L. Yin, and H. Vu, Phys. Rev. Lett. **94**, 0175003 (2005).
54. T. Obiki, R. Itatani, and Y. Otani, Phys. Rev. Lett. **20**, 184 (1968).
55. R. Drake and S. Batha, Phys. Fluids B **3**, 2936 (1991).
56. D. Villeneuve, K. Baker, R. Drake, B. Sleaford, B. LaFontaine, K. Estabrook, and M. Prasad, Phys. Rev. Lett. **71**, 368 (1993).
57. J. Fernandez, J. Cobble, B. Failor, D. Dubois, D. Montgomery, H. Rose, H. Vu, B. Wilde, M. Wilke, and R. Chrien, Phys. Rev. Lett. **77**, 2702 (1996).
58. R. Kirkwood, B. MacGowan, D. Montgomery, B. Afeyan, W. Kruer, J. Moody, K. Estabrook, C. Back, S. Glenzer, M. Blain, E. Williams, R. Berger, and B. Lasinski, Phys. Rev. Lett. **77**, 2706 (1996).
59. D. Montgomery, B. Afeyan, J. Cobble, J. Fernandez, M. Wilke, S. Glenzer, R. Kirkwood, B. MacGowan, J. Moody, E. Lindman, D. Munro, B. Wilde, H. Rose, D. Dubois, B. Bezzerides, and H. Vu, Phys. Plasmas **5**, 1973 (1998).
60. G. Bonnaud, D. Pesme, and R. Pellat, Phys. Fluids B **2**, 1618 (1990).
61. S. Karttunen, Phys. Rev. A **23**, 206 (1981).
62. J. Heikkinen and S. Karttunen, Phys. Fluids **29**, 1291 (1986).
63. B. Bezzerides, D. DuBois, and H. Rose, Phys. Rev. Lett. **70**, 2569 (1993).
64. B. Bezzerides, D. DuBois, H. Rose, and D. Russell, Phys. Scr. T **63**, 16 (1996).
65. R. Berger, C. Still, E. Williams, and A. Langdon, Phys. Plasmas **5**, 4337 (1998).
66. D. Russell, D. DuBois, and H. Rose, Phys. Plasmas **6**, 1294 (1999).

https://doi.org/10.1017/hpl.2014.50 Published online by Cambridge University Press

67. R. Yan, J. Li, and C. Ren, Phys. Plasmas **21**, 062705 (2014).
68. C. Riconda, S. Weber, V. Tikhonchuk, J.-C. Adam, and A. Heron, Phys. Plasmas **13**, 083103 (2006).
69. C. Riconda, S. Weber, O. Klimo, A. Heron, and V. Tikhonchuk, EPJ Web Conf. **59**, 05007 (2013).
70. H. Vu, D. DuBois, D. Russell, and J. Myatt, Phys. Plasmas **19**, 102708 (2012).
71. H. Vu, D. DuBois, J. Myatt, and D. Russell, Phys. Plasmas **19**, 102703 (2012).
72. H. Vu, D. DuBois, D. Russell, J. Myatt, and J. Zhang, Phys. Plasmas **21**, 042705 (2014).
73. S. Weber, C. Riconda, and V. Tikhonchuk, Phys. Rev. Lett. **94**, 055005 (2005).
74. R. Yan, C. Ren, J. Li, A. Maximov, W. Mori, Z.-M. Sheng, and F. Tsung, Phys. Rev. Lett. **108**, 175002 (2012).
75. J. Myatt, J. Zhang, R. Short, A. Maximov, W. Seka, D. Froula, D. Edgell, D. Michel, I. Igumenshchev, D. Hinkel, P. Michel, and J. Moody, Phys. Plasmas **21**, 055501 (2014).

https://doi.org/10.1017/hpl.2014.50 Published online by Cambridge University Press